Chemistry–A European Journal
Full Paper
doi.org/10.1002/chem.202103346

Chemistry Europe
European Chemical Societies Publishing

www.chemeurj.org

Highly Efficient Ir(III)-Coumarin Photo-Redox Catalyst for Synergetic Multi-Mode Cancer Photo-Therapy

Zhongxian Fan,[a] Jiaen Xie,[b] Tumpa Sadhukhan,[c] Chao Liang,[b] Can Huang,[a] Wenqing Li,[a] Tingxuan Li,[a] Pingyu Zhang,[b] Samya Banerjee,*[d] Krishnan Raghavachari,[c] and Huaiyi Huang*[a]

Abstract: Four photo-catalysts of the general formula [Ir(CO6/ppy)$_2$(L)]Cl where CO6 = coumarin 6 (**Ir1**–**Ir3**), ppy = 2-phenylpyridine (**Ir4**), L = 4′-(3,5-di-tert-butylphenyl)-2,2′:6′,2′′-terpyridine (**Ir1**), 4′-(3,5-bis(trifluoromethyl)phenyl)-2,2′:6′,2′′-terpyridine (**Ir2** and **Ir4**), and 4-([2,2′:6′,2′′-terpyridin]-4′-yl)-N,N-dimethylaniline (**Ir3**) were synthesized and characterized. These photostable photo-catalysts (**Ir1**–**Ir3**) showed strong visible light absorption between 400–550 nm. Upon light irradiation (465 and 525 nm), **Ir1**–**Ir3** generated singlet oxygen and induced rapidly photo-catalytic oxidation of cellular coenzymes NAD(P)H. **Ir1**–**Ir3** showed time-dependent cellular uptake with excellent intracellular retention efficiency. Upon green light irradiation (525 nm), **Ir2** provided a much higher photo-index (PI = 793) than the clinically used photosensitizer, 5-aminolevulinicacid (5-ALA, PI > 30) against HeLa cancer cells. The observed necro-apoptotic anticancer activity of **Ir2** was due to the **Ir2** triggered photo-induced intracellular redox imbalance (by NAD(P)H oxidation and ROS generation) and change in the mitochondrial membrane potential. Remarkably, **Ir2** showed in vivo photo-induced catalytic anticancer activity in mouse models.

Introduction

The first generation platinum-based chemotherapeutic drugs are now suffering from some drawbacks such as drug resistance and severe side effects.[1–2] Several important types of cancers have become resistant against the platinum-based chemotherapeutics.[3–4] Considering the prediction that the global burden of cancer patients and deaths in 2040 will increase up to 47 % from 2020, development of next generation cancer drugs which can overcome the drawbacks of platinum-based drugs are of supreme priority in the medicinal chemistry research.[5] Over the past few decades, photodynamic therapy (PDT), based on light, oxygen and photosensitizer (PS), is continuously showing promising tumor-targeting anticancer potential due to the accurate spatio-temporal control over the drug activation at the cancer site.[6–7] On light exposure, the excited state PSs are known to generate intracellular reactive oxygen species (ROS) such as superoxide radicals (via type I pathway) or singlet oxygen ($^1O_2$, via type II pathway).[6–7] The clinical organic photosensitizers are known show anticancer activity mainly via oxygen-dependent type II pathway and use of such photosensitizers are restricted due to side effects like skin photosensitivity and hepatotoxicity.[8–10] Moreover, the hypoxic microenvironment in the solid tumors is reported to drastically reduce the therapeutic effect of the organic PSs which rely mainly on highly oxygen-dependent type II photosensitization pathway.[11–13] Thus, now there is an urgent need of new generation photosensitizers which can work even at low oxygen concentration.[14–16]

In the last decade, several photoactive metal complexes with significant photo-stability, enhanced aqueous solubility and tunable photo-therapeutic efficiency have shown great potential as the new generation PSs for PDT.[17–22] In this context, Ir(III)-based PSs are of particular interest as these PSs can not only generate intracellular ROS but also can function as photo-catalysts for endogenous nicotinamide adenine dinucleotide (NADH) photo-oxidation.[23–24] It is important to discuss that the reduced nicotinamide adenine dinucleotide (NADH) has crucial role in the cellular metabolism such as in glycolysis and tricarboxylic acid cycle.[25,26] NADH is also the main electron source in the mitochondrial electron transport chain.[27,28] Moreover, the reduced nicotinamide adenine dinucleotide 2′-phosphate (NADPH) is another essential coenzyme in living cells considering its important role in many important cellular processes such as in bio-molecules synthesis and cellular

[a] *Z. Fan, C. Huang, W. Li, T. Li, Dr. H. Huang*
School of Pharmaceutical Science (Shenzhen)
Sun Yat-sen University
Guangzhou, 510275 (P. R. China)
E-mail: huanghy87@mail.sysu.edu.cn

[b] *J. Xie, C. Liang, Dr. P. Zhang*
College of Chemistry and Environmental Engineering
Shenzhen University
Shenzhen, 518060 (P. R. China)

[c] *Dr. T. Sadhukhan, Dr. K. Raghavachari*
Department of Chemistry
Indiana University, Bloomington
Indiana 47405 (USA)

[d] *Dr. S. Banerjee*
Department of Chemistry
Indian Institute of Technology (BHU)
Varanasi, UP-221005 (India)
E-mail: samya.chy@itbhu.ac.in

Supporting information for this article is available on the WWW under https://doi.org/10.1002/chem.202103346 metabolism.[29,30] Thus, intracellular NAD(P)H (NADH and NADPH) photo-oxidation, catalyzed by photoactive Ir(III) complexes can give rise to redox and metabolic disorder in cells and such methodology is expected to provide a new avenue for catalytic anticancer drug development. Recent reports from Sadler et al., and us already proved the feasibility of such anticancer mechanism of action.[23–24] This novel mechanism of drug action (MOA) can provide selectivity towards cancer cells over normal cells as Tedeschi et al., recently reported the significant upregulation of NAD(P)H concentration in cancer cells.[31] Important to note that NAD(P)H depletion by photoactive Ir(III) complexes in cancer cells may also provide a MOA to combat against tumor hypoxia-related drug resistance.[32,33]

In this newly emerging area of photo-catalytic cancer drug development research, one of the main challenges is to achieve photo-catalysis with longer wavelength light. For this purpose, the synthetic challenge is to develop Ir(III)-based photoactive complexes with strong absorption in visible light. Moreover, improvement of NADH photo-oxidation turnover frequency (TOF) and testing the anticancer efficacy of the above discussed mechanism against hypoxic tumors and tumor-containing mouse models are also two important issues in this research area. $[Ir(C^N)_2(N^N^N)]^+$ type complexes (Figure S1) are novel coordination saturated Ir(III) complexes reported in the recent years, which have been applied for nuclear histidine imaging (Ir–COOH), photodynamic therapy (Ir-tpypy and Ir-ES) and CO_2 detection (Ir-TP3).[34] However, $[Ir(C^N)_2(N^N^N)]^+$ type complexes have not yet been explored as photo-redox catalysts. Previously, our group have reported that coumarin-functionalized cyclometalated ligands can effectively improve the light absorption ability of traditional 2-phenylpyridine coordinated Ir(III) complexes.[24] Moreover, the trifluoromethyl group has shown great potential in the development of medicinal chemistry.[35] The above challenges encouraged us to carry out this work and herein, we design and synthesize novel coumarin coordinated photoactive Ir(III) complexes (**Ir1**–**Ir4**, Figure 1) with strong visible light absorption ability and photo-stability. **Ir4** with 2-phenylpyridine was introduced as a control to study the contribution of coumarin 6 ligand in photocatalysis and photo-cytotoxicity. Upon 525 nm green light irradiation, **Ir1**–**Ir3** photocatalytically oxidize intracellular NAD(P)H with significantly high TOF. The complexes on light exposure also generate intracellular hydrogen peroxide and singlet oxygen via type I and type II pathway, respectively. The remarkable necro-apoptotic anticancer activities of the complexes can be corelated with synergistic interactions of intracellular NAD(P)H photo-oxidation and ROS generation (Scheme 1). Importantly, **Ir2** exhibits very high photo-index (PI = 793), much higher compared to the clinically used photosensitizer, 5-aminolevulinicacid (5-ALA, PI > 30) against HeLa cells monolayer. Moreover, **Ir2** induces significantly photo-catalytic anticancer effect against the tumor bearing mice.

Results and Discussion

The tridentate ligands and Ir(III) complexes, **Ir1**–**Ir4** were prepared according to the reported methods with minor modification.[36] In brief, the complexes **Ir1**–**Ir3** were synthesized by refluxing coumarin 6-coordinated Ir(III) μ-chloro-bridged dimers and various tridentate ligands in $CHCl_3$/MeOH (3:1) for overnight. The complexes were purified by Al_2O_3 column chromatography. All the complexes were characterized by ^{1}H NMR and high-resolution mass spectrometry (HRMS) (Figure S2–S12).

The photophysical properties of the complexes were studied in various solvents to examine the influences of solvent polarity and viscosity. **Ir1**–**Ir3** showed a broad metal-to-ligand charge-transfer (MLCT) band between 400–550 nm (Figure 2A).[37–38] On the contrary, **Ir4** showed much weaker absorption above 400 nm in all the solvents (Figure S13). **Ir1**–**Ir3** exhibited broad and strong phosphorescence between 550–650 nm with moderate emission quantum yields compared with $Ru(bpy)_3Cl_2$ (Figure 2A, Table S1). Notably, the phosphorescence intensity of **Ir4** was too week to observe in all the tested solvents, indicating that coumarin 6 significantly enhances the phosphorescence property of **Ir1**–**Ir3** (Figure S13).

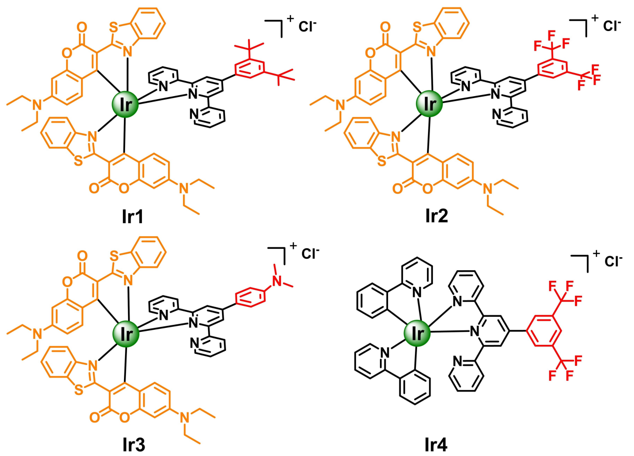

Figure 1. The chemical structure of **Ir1**–**Ir4**.

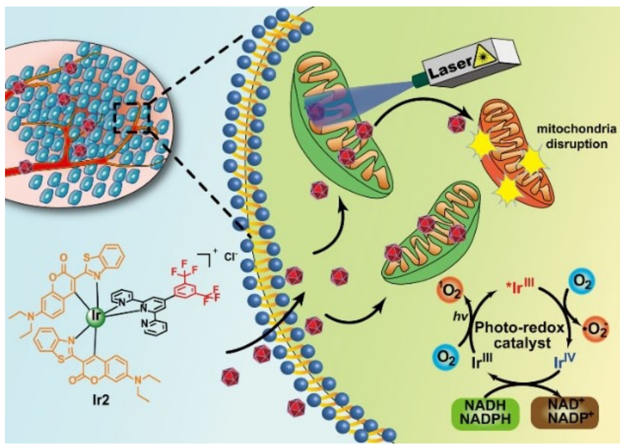

Scheme 1. Schematic illustration of **Ir2** induced photo-catalytic cancer cell death mechanism.

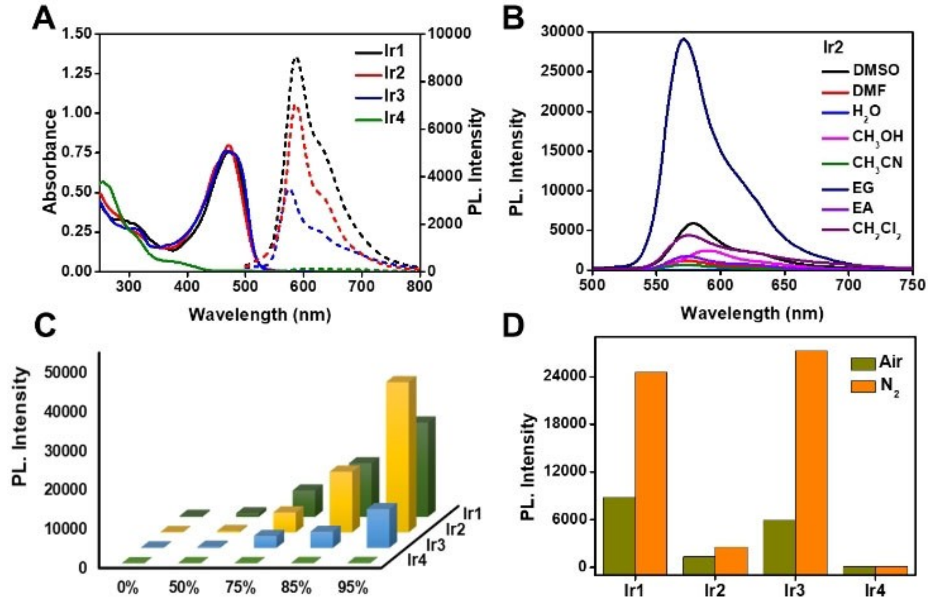

Figure 2. Photophysical properties of **Ir1**–**Ir4**. (A) Absorption and phosphorescence spectra of **Ir1**–**Ir4** (10 μM) in CH_2Cl_2. (B) Phosphorescence spectra of **Ir2** (10 μM) in different solvents at 298 K, $\lambda_{ex}=488$ nm. (C) Phosphorescence intensities of **Ir1**–**Ir4** (10 μM) at the emission maxima in glycerol-H_2O mixtures (0–95 % glycerol) at 298 K, $\lambda_{ex}=488$ nm. (D) Phosphorescence intensities of **Ir1**–**Ir4** (10 μM) at the emission maxima in aerated or nitrogen-saturated CH_2Cl_2 at 298 K, $\lambda_{ex}=488$ nm.

Besides, **Ir1**–**Ir3** exhibited polarity-sensitive phosphorescence, higher intensity in low polarity solvent such as CH_2Cl_2 (Figure 2B and S13). Interestingly, we found that **Ir1**–**Ir3** exhibited the highest intensity phosphorescence in ethylene glycol (EG, Figure 2B and S13). This observation inspired us to study the influence of solvent viscosity on phosphorescence of **Ir1**–**Ir4.** **Ir1**–**Ir3** exhibited viscosity-dependent phosphorescence in glycerol-H_2O mixtures (0-95 % glycerol, Figure 2C and S14), the higher the viscosity, higher was the phosphorescence. The viscosity-responsive phosphorescence of these complexes was due to the rotation of N, N-diethyl in the coumarin 6 ligand. This was evident from the fact that **Ir4** with the same 4′-(3,5-bis (trifluoromethyl)phenyl)-2,2′:6′,2′′-terpyridine ligand but without the coumarin 6 did not show similar viscosity-dependent phosphorescence (Figure 2C and S14). Moreover, the phosphorescence intensities and excited state lifetimes of the **Ir1**–**Ir3** were found to increase by ca. 3 and 2 times, respectively, in nitrogen-saturated solution compared to that in aerated solution. This observation indicated that **Ir1**–**Ir3** at the excited state can strongly interact with the oxygen (Figure 2D, S15 and Table S1). The interaction of triplet oxygen with the excited state of metal complexes has been recognized as an important process to generate reaction oxygen species (ROS) in photodynamic therapy.[6–7,16,18]

Ir1–**Ir4** in their cationic forms were modelled by density functional theory (DFT) calculations as presented in the Supporting Information (Figure S16, Table S2). The computed redox potentials indicated switching of the redox properties in the ground and excited states (Table S3). The frontier molecular orbitals (FMO) of ground state (S_0) (Figure S17) show that the FMOs are delocalized over the ligands and correspond to the $\pi\pi^*$ type with different contributions and some metal center (MC) character. Figure S18 shows that the lowest singly occupied molecular orbitals (LSOMO) are predominantly located on the metal center and one of the coumarin ligands for **Ir1** and **Ir2**, whereas the highest singly occupied molecular orbitals (HSOMO) are located on the metal center with less contribution from the second coumarin ligand. The $\Delta E_{\text{HSOMO-LSUMO}}$ for **Ir1** and **Ir2** is 1.80 eV which is comparable to the experimentally observed 2.0 eV of emission energy ($T_1 \rightarrow S_0$). The LSOMO to HSOMO transition is a mixed MLCT and $\pi\pi^*$ transition. For **Ir3**, the LSOMO is located on substituted tpy and HSOMO on the metal center and the coumarin ligand. For **Ir4**, the LSOMO and HSOMO are both located on the MC and ppy ligands. The natural transition orbitals (NTO) are represented in Figure S19. As the vertical $S_0 \rightarrow T_1$ excitation shown, the T_1 state is delocalized predominantly over the coumarin ligands for **Ir1** to **Ir3** and substituted ppy for **Ir4**, corresponding to the $\pi\pi^*$ excitation type mixed with some MLCT character with different contributions from different d-orbitals of Ir atom. Further, we estimated the emission energies with $(\Delta E_{\text{S-T}})_{\text{adiabatic}}$ (Table S2) and for **Ir1** to **Ir3** they deviate by ~0.4 eV since we have not considered spin-orbit coupling (SOC) and vibronic coupling in our calculations and the resulting T_1 state is an average over the three substates of the triplet.[39]

A good photosensitizer should have significantly high dark- and photo-stability for cellular application without any unwanted dark toxicity and photo-decomposition during irradiation.[16,18] We used ^{1}H NMR to monitor the stability of **Ir1**–**Ir3** in the dark for 72 h or after 465 nm light irradiation. The results showed that the ^{1}H NMR spectra of **Ir1**–**Ir3** remained almost unchanged in the dark even after 72 h. Moreover, **Ir1**–

Ir3 also showed excellent photo-stability without any notable photo-degradation under 465 nm light irradiation (Figure 3A and S20). Overall, the stability studies indicate that **Ir1**–**Ir3** have significantly high dark- as well as photo-stability and they can be studied as stable photosensitizers.

Ir(III)-based photosensitizers are known to generate singlet oxygen ($^1O_2$) in the solution and also in the cancer cells by an energy transfer process from triplet excited state of the Ir(III)-based photosensitizers to the $^3O_2$.[16–17,23–24,32] As we had observed a significant difference in the phosphorescence intensities and lifetimes of **Ir1**–**Ir3** in the presence or absence of triplet oxygen, we wanted to explore the $^1O_2$ generation ability of the complexes. We have monitored the change in the singlet oxygen sensor, 9,10-anthracenediyl-bis(methylene) dimalonic acid (ABDA)-based absorbance at 380 nm in the presence of **Ir1**–**Ir3** upon 465 nm and 525 nm irradiation.[40] **Ir1**–**Ir3** significantly induced $^1O_2$ generation after light irradiation as was evident from the decrease of ABDA-based absorbance (Figure 3B and S21). This observation depicted that the complexes could act as good photosensitizers and might have future as intracellular $^1O_2$ generator for photo-chemotherapeutics development.

We discussed in the introduction that any artificial alteration in the intracellular NADH or NADPH is expected to create intracellular redox imbalance and metabolic disorder, and ultimately can cause cell death.[41] In 2019, Sadler and coworkers for the first time delivered a novel Ir(III)-based photo-catalyst for intracellular NADH oxidation.[23] Our group very recently reported an Ir(III)-based photo-catalyst which not only catalyzed NAD(P)H oxidation in cancer cells but also showed excellent in vivo photochemotherapeutic effects.[24] Important to note that in both of these studies, 465 nm blue light was used and tissue penetration ability of blue light is considerably poor. Here we studied the efficiencies of **Ir1**–**Ir4** as the photo-catalysts for oxidation of NADH and NADPH by UV-visible spectroscopy in PBS. In the absence of light, the absorption spectra of NADH or NADPH did not change even after incubation with **Ir1**–**Ir4** (1 μM) for 30 min (Figure S22–S23). In contrast, upon photo-irradiation (465 nm and 525 nm), the absorbance of the NAD(P)H-based band at 339 nm was decreased gradually in the presence of **Ir1**–**Ir4** (0.5 μM for NADH oxidation and 1 μM for NADPH oxidation, respectively), indicating the ability of the complexes to induce photo-oxidation of NAD(P)H (Figure 3C and S22-S24A). The photo-oxidation of NAD(P)H was accompanied with H_2O_2 generation as was detected by the peroxide detection strips (inset figures, Figure S22–S24A). Interestingly, **Ir1**–**Ir3** induced NADH photo-oxidation (at 465 nm) with very high turnover number (TON = ca. 200) and turnover frequency (TOF = ca. 1200), almost 4–10 times and 12–25 times higher, respectively, than the previous reports (Table S4).[23] However, **Ir4** without the coumarin 6 did not induce NAD(P)H photo-oxidation under the same condition. At the excited state, **Ir3** ($[Ir^*]^+/[Ir]^0 = +0.24$ V, TOF $= 1357.2\ h^{-1}$) was much more reductive than **Ir1** ($+0.35$ V, TOF $= 1097.8\ h^{-1}$) and **Ir2** ($+0.54$ V,

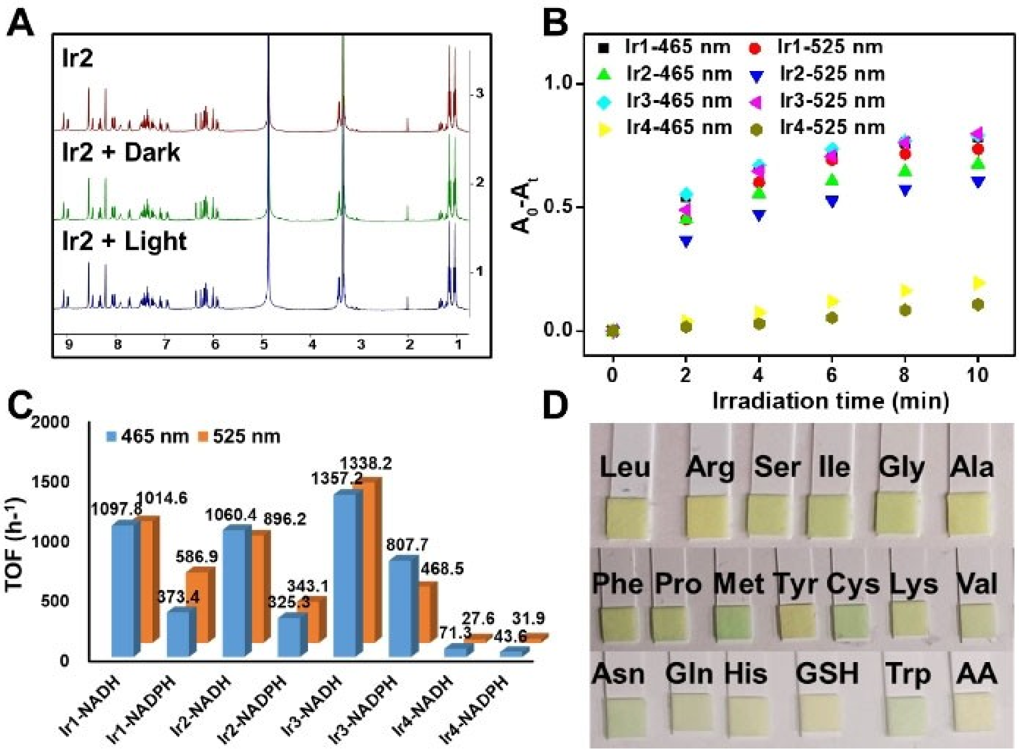

Figure 3. (A) ^1H NMR spectra of **Ir2** after 72 h incubation in the dark or irradiation (465 nm, 11.7 J/cm^2). (B) ABDA photodegradation at 380 nm by **Ir1**–**Ir4** (1 μM) in H_2O upon 465 nm (11.7 J/cm^2) and 525 nm (29.56 J/cm^2) light irradiation. (C) Turnover frequencies (TOF) of **Ir1**–**Ir4** for NADH (160 μM) or NADPH (160 μM) photo-oxidation at 465 nm (11.7 J/cm^2) or 525 nm (29.56 J/cm^2) light. (D) Photocatalytic generation of H_2O_2 in the presence of amino acids and **Ir2** (1 μM). AA = all amino acids in the dark.

TOF = 1060.4 h^{-1}), almost 10 times higher than the previously reported coordinated unsaturated NADH photo-catalyst, [Ir(ttpy)(pq)Cl]PF_6 (+0.66 V, TOF = 100.4 h^{-1})[23] (Table S4). The increase in reductive power increases the TOF and the increased phosphorescence intensity of **Ir1**–**Ir3** along with increasing concentration of NADH (Figure S24B) together confirmed that **Ir1**–Ir**3** mainly functionalized as excited state reductant rather than excited state oxidant such as in the case of [Ir(ttpy)(pq)Cl]PF_6.[23] Remarkably, **Ir1**–**Ir3** also photo-oxidized NADH upon 525 nm green light irradiation with similar efficiencies to that under 465 nm light. This finding is highly important considering the fact that tissue penetration power of 525 nm light is significantly higher than 465 nm light and hence deep-seated tumors could also be treated with our complexes. As these complexes exhibited polarity-dependent luminescence, it was meaningful to further compare the photo-catalytic activity of the complexes in different solvents of various polarity, but the high hydrophilic nature of NAD(P)H restricted such exploration. Moreover, despite of functioning as an excellent photo-catalyst for NAD(P)H oxidation, **Ir2** also induced photo-catalytic oxidation of several amino acids, followed by H_2O_2 generation (Figure 3D). The exact mechanism of oxidation and oxidized products are not well understood and these will be subject of our future research.

The ability of the complexes to induce $^1O_2$ generation and photo-oxidation of NAD(P)H on 465 nm and 525 nm light irradiation inspired us to explore the possibility of the complexes as PDT agents. MTT assay[42–44] was used to investigate the dark- and photo-cytotoxicity of **Ir1**–Ir**4** against human cervical cancer cell line (HeLa), epidermoid carcinoma cell line (A431), human nasopharyngeal epithelial cell line (NP69) and mouse melanoma cell line (B16). The clinical chemotherapy drug cisplatin and PDT drug 5-aminolevulinic acid (5-ALA) were used as positive controls for the dark- and photo-therapy experiments, respectively. For the dark experiments, cells were incubated with various drugs (**Ir1**–Ir**4**, cisplatin and 5-ALA) for 4 h and then the cells were allowed to grow in fresh cell culture medium for 44 h in the dark. The light groups were irradiated with 465 nm (11.7 J/cm^2) or 525 nm (29.56 J/cm^2) light, immediately after drug incubation. The dark and light IC_{50} values of the complexes against various cancer cell lines are listed in Table S5. The reduced cytotoxicity of cisplatin was probably due to the short-term incubation (4 h).[42,45–47] Upon 465 nm light irradiation, **Ir1**–**Ir3** exhibited much higher photo-cytotoxicity index (PI, PI = $IC_{50\ dark}/IC_{50\ light}$) than 5-ALA (PI = 23–793 for **Ir1**–**Ir3** vs. 22.37–29.63 for 5-ALA) against various cancer cell lines. Interestingly, **Ir2** gave a light IC_{50} value of ca. 30 nM against HeLa cells with an excellent PI of ca. 793. Remarkably, **Ir1**–**Ir3** were also highly anticancer active ($IC_{50\ light}$ = 10 nM–0.4 μM) when irradiated with 525 nm light. This indicates that judicial choice of ligands can provide photo-cytotoxicity at longer wavelength light. This finding is highly important considering the higher tissue penetration ability of green light in comparison to the blue light.[16,18] The control complex, **Ir4**, was much less active compared to **Ir1**–**Ir3**, indicating coumarin 6 has a significant role in the augmentation of the photo-cytotoxicity of **Ir1**–**Ir3**. Overall, our results indicate that the complexes **Ir1**–**Ir3** (especially **Ir2**) have prospects as PDT agents at nM dose.

Cellular uptake is a highly important factor which controls the activity of drug candidates and their successful clinical applications.[48] The introduction of coumarin 6 ligand increased the lipophilicity of the complexes (Figure 4A). The increased lipophilicity may in turn enhance the intracellular accumulation and retention in cancer cells.[49,50] We studied the cellular uptake of **Ir1**–**Ir3** in HeLa cells using flow cytometry. As shown in Figure 4B and S25, cellular uptake of **Ir1**–**Ir3** was found to be time-dependent. In general, drug molecules are known to be taken up by living cells either by an energy-dependent pathway (endocytosis, active transport) or an energy-independent pathway (facilitated diffusion, passive diffusion).[51] The cell membrane potential is generally linked to the cellular uptake.[51] To investigate the effect of the cell membrane potential on the intracellular uptake, we either reduced the membrane potential by using a high potassium ions environment (170 mM) or increased the membrane potential using valinomycin. As shown in the Figure 4C and S26, HeLa cells that were pretreated with endocytosis inhibitors such as NH_4Cl and chlorpromazine, did not show any significant decrease in the **Ir1**–**Ir3** based intracellular emission intensity, indicating that **Ir1**–**Ir3** did not enter into the cells via an endocytosis pathway. No obvious reduction of intracellular **Ir1**–**Ir3** uptake was observed at the high or low K^+ concentration compared to that of the control. Interestingly, incubation at 4 °C significantly reduced the uptake of **Ir1**–**Ir3**, indicating that an energy-dependent pathway is possibly responsible for the cellular uptake. In cells, adenosine triphosphate (ATP) transports energy for metabolism.[52] To confirm the energy-dependent cellular uptake of **Ir1**–**Ir3**, an ATP-depleted cellular environment in HeLa cells was generated by 2-deoxy-D-glucose (a glucose analogue that inhibits glycolysis) and oligomycin (an inhibitor of oxidative phosphorylation).[53,54] Under such ATP-depleted conditions, the intracellular emission intensity decreased compared to control group, illustrating that **Ir1**–**Ir3** enter into the cells via an energy-dependent pathway (Figure 4C and S26).

It is important to note that not only the cellular uptake, but also the intracellular retention efficiency is a vital factor to effect drug action.[55] To study the intracellular retention of the complexes, HeLa cells were incubated with **Ir1**–**Ir3** for 4 h followed by PBS washing and incubation in fresh medium. Cells were collected for intracellular emission intensity analysis by flow cytometry at various time points. The result shown in Figure 4D and S25 indicates that the intracellular emission intensity in **Ir1**–**Ir3** treated HeLa cells did not decrease even after 6 h of drug-containing medium removal. This study indicates that the excretion of internalized **Ir1**–**Ir3** from the cells is negligible which might be useful to avoid drug resistance.[55] It is worthy to mention that one of the main reasons behind the cisplatin's resistance is pumping out of cisplatin by cancer cells.[2,45,48] Taken together, these results indicate that **Ir1**–**Ir3** exhibited good intracellular accumulation and retention efficiency in cancer cells.

The intracellular localization of anticancer agents controls the MOA significantly.[56] In recent years, anticancer agents with

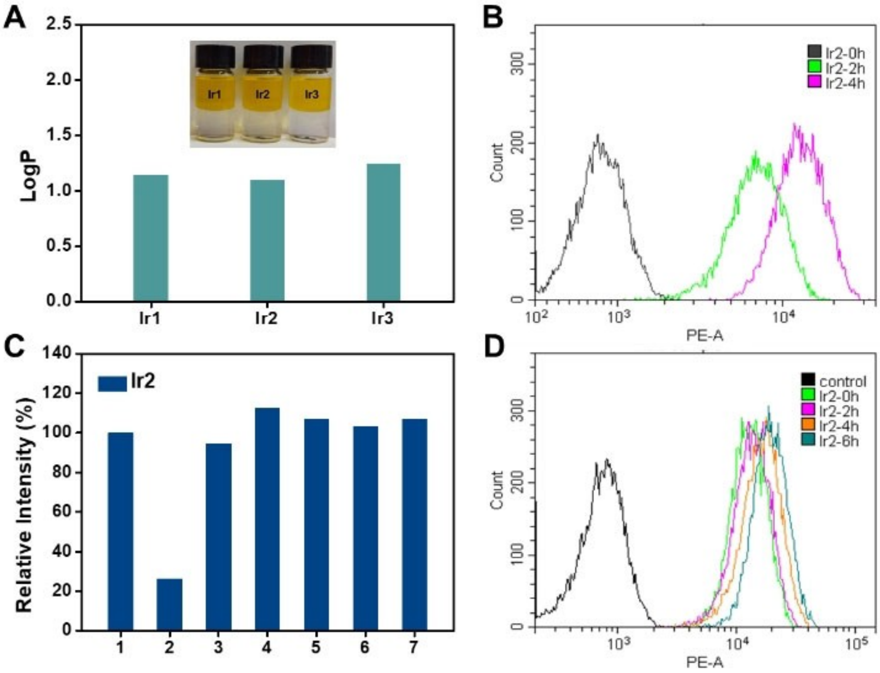

Figure 4. Intracellular uptake and retention efficacy of **Ir2** in HeLa cells. (A) The octanol/water partition coefficients of **Ir1**–**Ir3**. Inset: the distributions of **Ir1**–**Ir3** in octanol/water mixture. (B) Quantitative analysis of the cellular uptake of **Ir2** in HeLa cells after incubation with **Ir2** (10 μM) at different durations. (C) Intercellular emission intensity of HeLa cells incubated with **Ir2** (5 μM) in the presence of cellular uptake inhibitors: 1) control cells at 37 °C, 2) cells at 4 °C, 3) metabolic inhibitors, 4) 50 mM NH_4Cl, 5) 10 μM chlorpromazine, 6) high K^+-HBSS buffer (170 mM K^+), 7) 50 μM valinomycin (containing 5.8 mM K^+). (D) Quantitative analysis of the retention efficiency of **Ir2** in HeLa cells after incubation with **Ir2** (10 μM) for different durations.

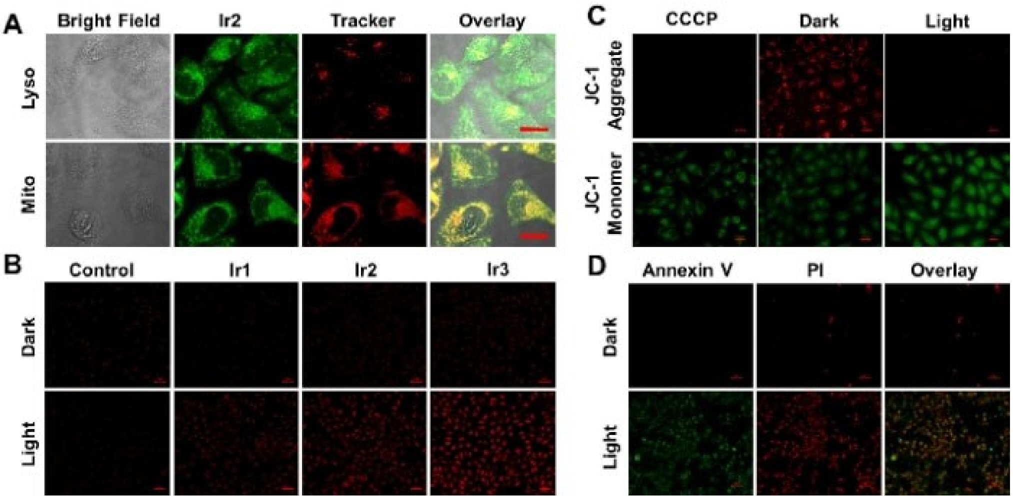

Figure 5. (A) Intracellular localization of **Ir2** in HeLa cells after incubation with **Ir2** (10 μM) for 2 h followed by co-staining with mito-tracker and lyso-tracker dyes (100 nM) for 20 min. $\lambda_{ex}/\lambda_{em}$: 488/600 nm for **Ir2** and 633/680 nm for mitotracker and lysotracker, scale bar: 20 μm. (B) Light induced superoxide generation by **Ir1**–**Ir3** (0.01 μM) as was by the DHE probe, scale bar: 50 μm. (C) **Ir2** (0.25 μM) induced change in the mitochondrial membrane potential of HeLa cells after dark or light treatment, scale bar: 20 μm. (D) Annexin V-FITC and PI dual fluorescence imaging, indicating necro-apoptotic HeLa cells death induced by **Ir2** (2.5 μM) upon light exposure, scale bar: 50 μm.

selective localization in a particular cellular organelle (other than cell nucleus) have attracted significant attention.[23,24,43,44,57,58] Such molecules may have the potential to overcome the drug resistance problem of platins.[57] To study the intracellular localization of our complexes, we used mitotracker deep-red and lysotracker red to stain the mitochondria and lysosomes, respectively. As shown in Figure 5A, after treatment with the complex **Ir2**, the intracellular **Ir2**-based green emission in HeLa cells mostly merged with the red fluorescence of the mitotracker. In comparison, the green emission of **Ir2** had significantly less overlap with the lysotracker. Similar results were also observed with **Ir1** and **Ir3** in HeLa cells (Figure S27). Overall, it is evident from the cellular localization study that **Ir1**–**Ir3** mainly localize at the mitochondria. Such mitochondrial localization is highly important to achieve notable anticancer activity as mitochondria play an important role in many cellular operations, such as the generation of energy, maintaining intracellular redox balance and metabolism. Thus, any damage in mitochondria by our complexes is expected to induce cell death.[23,24,27,28,30,59]

As our complexes generated H_2O_2 during the photo-induced oxidation of NAD(P)H, we tested the prospect of **Ir1**–**Ir3** as the photo-induced cellular superoxide generators. The O_2^- levels in HeLa cells were measured by dihydroethidium (DHE) probe[60] after treating with **Ir1**–**Ir3**. As shown in Figure 5B, DHE fluorescence intensity was significantly enhanced in **Ir1**–**Ir3** treated HeLa cells but only after 465 nm light irradiation, indicating photo-induced superoxide generation ability of our complexes. Such intracellular superoxide generation is expected to induce oxidative stress in cells and ultimately can cause cell death. To investigate whether loss of mitochondrial membrane integrity is happening during the cell death caused by **Ir1**–**Ir3**, JC-1 assay was performed.[61] As shown in Figure 5C, **Ir2** induced loss of MMP in HeLa cells upon light irradiation as was evident from the significant decrease in the red fluorescence compared to that of the non-irradiated control cells. Thus, the photo-induced cell death, induced by **Ir1**–**Ir3** in HeLa cells, involved depolarization of mitochondrial membrane. The disruption of mitochondrial membrane potential (MMP) is connected to the early stage of apoptosis.[62,63] To study whether apoptosis is the pathway of cell death or not, annexin V-FITC/propidium iodide (PI) co-staining was conducted.[24] The dark or light control cells and the cells treated with **Ir1**–**Ir3** in the dark were not stained by annexin V-FITC or PI, indicating that the cells were alive. But, a significant fraction of **Ir1**–**Ir3** treated cells, on light irradiation, were stained only by annexin V-FITC, revealing early apoptosis. Another significant fraction of the cells was co-stained by annexin V-FITC and PI, indicating late apoptosis and/or necrosis (Figure 5D and S28).

Based on the outstanding in vitro photo-activated anticancer activities of **Ir2**, we further evaluated its in vivo photo-chemotherapeutic efficacy against tumor bearing mice via intratumor injection. A431 (epidermoid carcinoma) bearing mice model was selected as an in vivo model to establish orthotopically subcutaneous transplanted model. As shown in Figure 6A–D, **Ir2** + light group effectively reduced the size of the tumors in comparison to that of the controls group. Further results of H&E staining and TUNEL assays of mice tumor tissue (Figure 6E) indicated that **Ir2** + light treatment induced significant increasing of cell apoptosis and necrosis in contrast with control and only **Ir2** or light treatment. These results demonstrated the potential of **Ir2** as a highly efficient in vivo photochemotherapeutic agent.

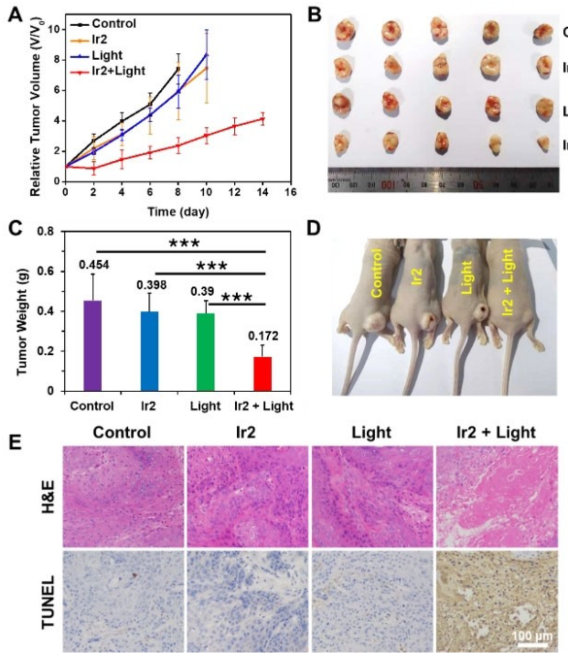

Figure 6. In vivo photo-chemotherapeutic activity of **Ir2** against A431 mice model. (A) Relative tumor growth curves of mice after various treatments. Control group: mice treated with PBS in the dark; **Ir2** group: mice treated with **Ir2** in the dark; light control group: mice treated with PBS and received light irradiation; **Ir2** + light group: mice treated with **Ir2** and received light irradiation. (B) Pictures of tumors collected from mice of different groups on the 14th d after various treatments. (C) Averaged weights of tumors shown in (B) (***$p < 0.001$, **$p < 0.01$, or *$p < 0.05$). (D) Pictures of mice bearing A431 tumors of different groups on the 14th d after various treatments. (E) H&E staining images and TUNEL assay images of tumor tissue of mice after various treatments. Scale bar: 100 μm.

Conclusion

We reported here Ir(III)-coumarin complexes with interesting tunable photophysical properties as highly efficient in vivo photo-chemotherapeutics for catalytic cancer treatment. The photo-chemotherapeutic activity of these complexes is due to their photo-induced NAD(P)H oxidation and ROS generation abilities which in turn created intracellular redox imbalance and inhibited ATP productions. These complexes generated intracellular ROS via both type I as well as type II pathways. In aqueous media, **Ir1**–**Ir3** catalyzed NAD(P)H oxidation on 465 nm light irradiation with extremely high TON and TOF, much higher compared to that of the earlier reports.[23,24] Interestingly, the complexes also effected highly efficient NAD(P)H oxidation induced by 525 nm green light. To the best of our knowledge, this is the first report of green light induced NAD(P)H photo-oxidation by metal complexes in aqueous media. **Ir1**–**Ir3** entered into the cells by an energy-dependent pathway. The complexes preferably localized in the mitochondria with significantly high intracellular retention, indicating that these complexes may overcome the problem of drug resistance. These complexes were highly effective as in vitro and in vivo photo-cytotoxic agents against various types of cancers under light irradiation. Thus, overall, this study is a significant milestone towards the development of photocatalytic drugs which can work even under longer wavelengths.

Experimental Section

Materials: $IrCl_3 \cdot 3H_2O$, 3,5-di-tert-butylbenzaldehyde, coumarin 6, 3,5-bis(trifluoromethyl)benzaldehyde, 9,10-anthracenediyl-bis (methylene) dimalonic acid (ABDA) and 2-phenylpyridine were purchased from Bidepharm. 4-(Dimethylamino)benzaldehyde were purchased from Aladdin. 3-(4,5-dimethylthiazol-2-yl)-2,5-diphenyltetrazolium bromide (MTT) was purchased from Macklin. Human cervical cancer cell line (HeLa) and human nasopharyngeal epithelial cell line (NP69) were obtained from Sun Yat-Sen University (Guangzhou, China). Mouse melanoma cell line (B16) was obtained from Shanghai QiDa Biotechnology. Epidermoid carcinoma cell line (A431) was obtained from Procell Life Science & Technology Co. Ltd. Dulbecco Modified Eagle Medium (DMEM), Roswell Park Memorial Institute 1640 Medium (RPMI 1640), fetal bovine serum (FBS), penicillin/streptomycin were bought from Gibco. β-Nicotinamide adenine dinucleotide, reduced disodium salt I (β-NADH) and β-Nicotinamide adenine dinucleotide phosphate, reduced disodium salt II (β-NADPH) were purchased from Sigma-Aldrich. Mito-tracker®Red, Lsyo-Tracker®Deep Red and JC-1 was purchased from Life Technologies Corporation. Annexin V-FITC/PI Apoptosis Detection Kit and Dihydroethidium (DHE) was purchased from Beyotime Biotechnology.

Instruments: ^1H NMR spectra were recorded on Bruker AvanceIII-400. Positive ion HR-ESI-MS spectra were obtained by LCMS-IT-TOF (Shimadzu). UV-Visible absorption spectra were recorded on a PerkinElmer Lambda 600 UV-vis spectrophotometer. The fluorescence spectra and the emission quantum yield measurements were recorded on a Techcomp FL970 fluorescence spectrophotometer. Confocal microscopy was done with the by laser confocal microscopy (LCSM 880, Carl Zeiss, Göttingen, Germany).

Synthesis

Synthesis of tpy ligands: The terpyridine ligands **L1**–**L3** were prepared from the respective reaction of benzaldehyde with corresponding substituents (10 mmol), NaOH (37.5 mmol) and 2-acetylpyridine (20 mmol) in a mixture of ethanol (50 mL) and 28% $NH_3 \cdot H_2O$ (30 mL) at room temperature. After 4 h, the precipitate was filtered off and washed with water and cold ethanol, followed by drying under vacuum.

L1 (4′-(3,5-di-tert-butylphenyl)-2,2′:6′,2′′-terpyridine): ^1H NMR (400 MHz, Chloroform-*d*) δ 8.72 (s, 1H), 8.68 (d, *J* = 4.8 Hz, 2H), 7.67 (q, *J* = 7.9 Hz, 4H), 7.36 (s, 1H), 7.21 (t, *J* = 5.8 Hz, 2H), 5.42 (d, *J* = 3.3 Hz, 2H), 4.72 (t, *J* = 3.8 Hz, 1H), 1.35 (s, 18H).

L2 (4′-(3,5-bis(trifluoromethyl)phenyl)-2,2′:6′,2′′-terpyridine): ^1H NMR (400 MHz, Chloroform-*d*) δ 8.75 (ddd, *J* = 4.8, 1.7, 0.9 Hz, 2H), 8.74 (s, 2H), 8.69 (d, *J* = 8.0 Hz, 2H), 8.30 (s, 2H), 7.98 (s, 1H), 7.91 (td, *J* = 7.8, 1.8 Hz, 2H), 7.39 (ddd, *J* = 7.5, 4.8, 1.1 Hz, 2H).

L3 (4-([2,2′:6′,2′′-terpyridin]-4′-yl)-N,N-dimethylaniline): ^1H NMR (400 MHz, Chloroform-*d*) δ 8.75–8.72 (m, 2H), 8.71 (s, 2H), 8.66 (d, *J* = 8.0 Hz, 2H), 7.87 (td, *J* = 8.4, 2.1 Hz, 4H), 7.36–7.32 (m, 2H), 6.82 (d, *J* = 9.0 Hz, 2H), 3.05 (s, 6H).

Synthesis of Ir(III) μ-chloro-bridged dimer: $[Ir(CO6)_2Cl]_2$ dimers were synthesized from the reaction of iridium(III) chloride trihydrate (0.10 g, 0.28 mmol) and coumarin 6 (0.20 g, 0.58 mmol) in 2-ethoxyethanol/water (16 mL; 3:1 v/v) at 110 °C for 24 h. After cooling the reaction mixture to room temperature, the precipitate was filtered off and washed with ethanol and ethyl acetate. The resulting orange solids were dried under vacuum to yield ca. 74% of Ir(III) μ-chloro-bridged dimer complexes (0.20 g, 0.11 mmol). $[Ir(ppy)_2Cl]_2$ dimer was obtained as yellow solids from the reaction of iridium(III) chloride trihydrate and 2-phenylpyridine in the above mentioned way.

***Synthesis of* Ir1–Ir4**: Complexes **Ir1**–**Ir4** were prepared by treating $[Ir(CO6)_2Cl]_2$ or $[Ir(ppy)_2Cl]_2$ with 2 equivalents of tpy ligand **L1**–**L3** in $CHCl_3$/MeOH (3:1; v/v) under refluxing condition (at 60 °C) for 12 h. The solvent of the reaction mixture was removed by distillation under reduced pressure, and the resulting solids were extracted with dichloromethane and water. The solvent of the organic layer was removed under vacuum. The obtained crude products were purified by column chromatography on neutral alumina (solvent: methanol/dichloromethane = 1/20). All the Ir(III) complexes were further characterized by HRMS and ^1H NMR.

Complex Ir1: Yield: 63%. ^1H NMR (400 MHz, Methanol-*d4*) δ 8.93 (d, J = 8.1 Hz, 1H), 8.79 (d, J = 1.7 Hz, 1H), 8.42 (d, J = 5.3 Hz, 1H), 8.30–8.25 (m, 1H), 8.05 (d, J = 8.0 Hz, 1H), 8.00 (d, J = 8.2 Hz, 1H), 7.97 (d, J = 1.7 Hz, 1H), 7.90 (s, 1H), 7.69–7.64 (m, 2H), 7.62 (d, J = 1.6 Hz, 2H), 7.48 (d, J = 8.5 Hz, 1H), 7.40 (t, J = 7.8 Hz, 1H), 7.35–7.28 (m, 2H), 7.24 (t, J = 7.8 Hz, 1H), 7.17–7.09 (m, 1H), 7.09–7.04 (m, 1H), 6.89 (dd, J = 7.5, 5.0 Hz, 1H), 6.31 (d, J = 2.5 Hz, 1H), 6.21 (d, J = 2.4 Hz, 1H), 6.19–6.13 (m, 2H), 6.10 (dd, J = 9.5, 2.5 Hz, 1H), 6.02 (d, J = 9.5 Hz, 1H), 5.90 (dd, J = 9.5, 2.6 Hz, 1H), 3.38 (q, J = 7.3 Hz, 4H), 3.29 (d, J = 8.8 Hz, 4H), 1.39 (s, 18H), 1.11 (t, J = 7.0 Hz, 6H), 1.01 (t, J = 7.0 Hz, 6H). HR-MS: $[M-Cl]^+$ calcd for $C_{69}H_{65}IrN_7O_4S_2^+$: 1312.4166, found: 1312.4333.

Complex Ir2: Yield: 67%. ^1H NMR (400 MHz, Methanol-*d4*) δ 9.07 (d, J = 1.9 Hz, 1H), 8.99 (d, J = 8.2 Hz, 1H), 8.56 (s, 2H), 8.47 (d, J = 5.0 Hz, 1H), 8.32 (td, J = 9.2, 8.2, 1.4 Hz, 1H), 8.21 (d, J = 1.6 Hz, 2H), 8.07 (d, J = 8.0 Hz, 1H), 8.02 (d, J = 7.9 Hz, 1H), 7.90 (s, 1H), 7.76–7.69 (m, 1H), 7.48 (d, J = 8.4 Hz, 1H), 7.42 (t, J = 7.5 Hz, 1H), 7.34 (q, J = 7.6 Hz, 2H), 7.27–7.14 (m, 2H), 7.12–7.04 (m, 1H), 6.98–6.89 (m, 1H), 6.35 (d, J = 2.5 Hz, 1H), 6.25 (d, J = 2.5 Hz, 1H), 6.19 (d, J = 9.4 Hz, 1H), 6.13 (dd, J = 8.8, 3.5 Hz, 2H), 6.00 (d, J = 9.5 Hz, 1H), 5.91 (dd, J = 9.5, 2.5 Hz, 1H), 3.41 (q, J = 7.2 Hz, 4H), 3.30 (d, J = 7.0 Hz, 4H), 1.14 (t, J = 7.0 Hz, 6H), 1.04 (t, J = 7.0 Hz, 6H). HR-ESI-MS: $[M-Cl]^+$ calcd for $C_{63}H_{47}F_6IrN_7O_4S_2^+$: 1336.2661, found: 1336.2842.

Complex Ir3: Yield: 59%. ^1H NMR (400 MHz, Methanol-*d4*) δ 8.90 (d, J = 8.2 Hz, 1H), 8.81 (d, J = 1.8 Hz, 1H), 8.41 (d, J = 5.5 Hz, 1H), 8.28 (t, J = 7.9 Hz, 1H), 8.05 (d, J = 7.9 Hz, 1H), 8.01 (d, J = 7.9 Hz, 1H), 7.86 (dd, J = 5.4, 3.5 Hz, 4H), 7.67–7.63 (m, 1H), 7.47 (d, J = 8.9 Hz, 1H), 7.40 (t, J = 7.6 Hz, 1H), 7.32 (t, J = 7.6 Hz, 1H), 7.27–7.23 (m, 1H), 7.21 (d, J = 7.6 Hz, 1H), 7.14 (s, 1H), 7.05 (t, J = 7.8 Hz, 1H), 6.91 (dd, J = 7.8, 4.8 Hz, 1H), 6.80 (d, J = 9.0 Hz, 2H), 6.31 (d, J = 2.4 Hz, 1H), 6.21 (d, J = 2.4 Hz, 1H), 6.17–6.12 (m, 2H), 6.08 (dd, J = 9.5, 2.5 Hz, 1H), 5.99 (d, J = 9.5 Hz, 1H), 5.91 (dd, J = 9.6, 2.5 Hz, 1H), 3.41–3.35 (m, 4H), 3.31–3.26 (m, 4H), 3.06 (s, 6H), 1.12 (t, J = 7.1 Hz, 6H), 1.02 (t, J = 7.0 Hz, 6H). HR-ESI-MS: $[M-Cl]^+$ calcd for $C_{63}H_{54}IrN_8O_4S_2^+$: 1243.3335, found: 1243.3465.

Complex Ir4: Yield: 72%. ^1H NMR (400 MHz, Chloroform-*d*) δ 10.06 (d, *J* = 8.3 Hz, 1H), 9.94 (d, *J* = 1.8 Hz, 1H), 8.82 (d, *J* = 5.5 Hz, 1H), 8.68 (s, 2H), 8.40 (td, *J* = 8.0, 1.5 Hz, 1H), 8.26 (d, *J* = 4.8 Hz, 1H), 8.01 (s, 1H), 7.91–7.76 (m, 4H), 7.75–7.70 (m, 1H), 7.58 (dd, *J* = 5.7, 1.4 Hz, 2H), 7.54 (d, *J* = 5.8 Hz, 1H), 7.40–7.31 (m, 2H), 7.16 (ddd, *J* = 7.2, 6.0, 1.4 Hz, 1H), 7.09 (dtd, *J* = 7.2, 4.3, 3.8, 1.8 Hz, 2H), 7.00–6.86 (m, 2H), 6.81–6.74 (m, 1H), 6.67–6.59 (m, 1H), 6.54 (d, *J* = 7.6 Hz, 1H), 6.39–6.30 (m, 1H), 5.88 (d, *J* = 7.7 Hz, 1H), 5.50 (d, *J* = 7.6 Hz, 1H). $C_{45}H_{29}IrN_5F_6^+$: 946.1954, found: 946.2003.

UV-vis and photoluminescence spectroscopy: PerkinElmer Lambda 600 UV-vis spectrophotometer and Techcomp FL970 fluorescence spectrophotometer were used with 1-cm path length quartz cuvettes. Spectra were processed using origin software. The UV-vis spectra of **Ir1**–**Ir4** (10 μM) in different solvents were taken at 293 K from 700 to 250 nm. The complexes (10 μM) in different solvents were excited at λ_{ex} = 488 nm in air at 298 K and recorded from 800 to 500 nm. The hypoxia photoluminescence spectra of **Ir1–Ir4** (10 μM) in CH_2Cl_2 were obtained after N_2 purging into solution for 5 min.

Phosphorescence quantum yields and lifetime measurements: Phosphorescence quantum yields were measured using a Techcomp FL970 fluorescence spectrophotometer. **Ir1–Ir3** were diluted to achieve an absorbance = 0.1 at 450 nm in CH_2Cl_2 or PBS. The complexes were excited at 450 nm under air at 298 K. Quantum yields in CH_2Cl_2 or PBS were determined by comparison with the emission of $[Ru(bpy)_3]Cl_2$ in CH_2Cl_2 or PBS and calculated using the following equation.

$$\Phi_x = \Phi_s \times (F_x/F_s) \times (A_s/A_x) \times (n_x/n_s)^2$$

Where Φ represents quantum yield; F stands for integrated area under the corrected emission spectrum; A is absorbance at 450 nm, the excitation wavelength; n is the refractive index of the solution; and the subscripts x and s refer to the complex sample and the standard, respectively.

Phosphorescence lifetime measurements were carried out using a combined photoluminescence lifetime and steady state spectrometer (FLS1000, Edinburgh Instruments Ltd) equipped with 450 nm pulsed diode NanoLED light source and the measurements were stopped after gathering 5000 counts of excited state species. The raw data were acquired and analyzed with Fluoracle software.

Viscosity-sensitive photoluminescence of Ir1–Ir4: The photoluminescence spectra of **Ir1–Ir4** in glycerol/water (0–100% glycerol) were recorded by Techcomp FL970 fluorescence spectrophotometer with 1 cm path-length quartz cuvettes, and the data was processed using Origin software.

Computational details: The Ir complexes in their monocationic form was studied by density functional theory (DFT) using the Gaussian 16 quantum chemistry package[64] and the optimized structures are presented in Figure S16. For geometry optimization, LANL2DZ with LANL2 pseudopotential basis set was employed for Ir and 6-31G(d) for all other atoms coupled with B3LYP-D3BJ as functional. The optimized geometries were confirmed to be local minima with no imaginary frequencies and the ground singlet (S1) and first excited triplet state (T1) geometries were obtained following restricted and unrestricted DFT respectively in vacuum.

To evaluate the energies CPCM implicit solvent model with dichloromethane (DCM) (ε = 8.93) as solvent, was chosen for transition energies and redox potentials as discussed below. Excited electronic states were obtained by time-dependent (TD) linear response calculations in DCM, and they are presented in Table S2, S3. We used range-separated functional CAM-B3LYP and LANL2DZ with LANL2 pseudopotential basis set for Ir and 6-31 + G(d,p) basis set for all other atoms.

To calculated the redox and photo-redox potentials of the complexes we used the vacuum correction to Gibbs free energy obtained from B3LYP-D3BJ geometry optimization and electronic energy calculated using B3LYP-D3BJ in DCM using LANL2DZ with LANL2 pseudopotential basis set for Ir and 6-31 + G(d,p) basis set for all other atoms. The Gibbs free energies of the singlet and triplet states relative to the optimized ionized and attached electronic states were computed. Absolute standard potentials were calculated from the solvated free energies at 293 K by,

$$E^0_{abs} = -\frac{\Delta G_{red}(sol)}{nF} - 0.03766$$

where n represents the number of electrons transferred, here n = 1, F is the Faraday constant, and ΔGred(sol) is the Gibbs free energy for the solvated reduction half-reaction (obtained by the appropriate Born-Haber type cycle), and the last term arises for the Gibbs free electron correction at 293 K. The reported redox potentials are versus Ag/AgCl.

Photo- and dark-stability study: Stability studies were carried out by ^{1}H NMR method using a Bruker AvanceIII-400 machine. ^{1}H NMR samples were prepared in MeOD and ^{1}H NMR spectra were monitored after 72 h in the dark or after 5 min of 465 nm light irradiation at 298 K.

Lipophilicity determination: The individual complexes (**Ir1–Ir3**) were added to 2.5 mL water-saturated n-octanol. The final concentration of the complex in solution was 40 μM. Then same amount of aqueous solution saturated with n-octanol was added to the complex solution. The resultant mixture was mixed thoroughly and vibrated at a constant temperature oscillator for 24 h. After stationary, the two-phase solutions were dispersed in 96-well plate and the complexes were quantified using the absorbance of 488 nm band. The calculation formula: logP = the concentration of complex in octanol phase/the concentration of complex in water phase.

Photocatalytic oxidation of NAD(P)H and detection of H_2O_2 generation: Reactions between **Ir1–Ir4** and NAD(P)H in PBS at different duration of irradiation with 465 nm light (11.7 J/cm^2) or 525 nm light (29.56 J/cm^2) were monitored by UV-vis spectroscopy at 298 K. The concentration of NADH and NADPH was obtained using the extinction coefficient $\varepsilon_{339} = 6220\ M^{-1}cm^{-1}$ and $\varepsilon_{339} = 6300\ M^{-1}cm^{-1}$, respectively. Furthermore, H_2O_2 generation during the reaction was detected by quantofix® peroxide test sticks (Sigma). The turnover number of catalysis was calculated using the following equations:

$$[NAD(P)^+] = [Abs(339\,nm)_{initial}\text{-}Abs(339\,nm)_{final}]/Abs(399\,nm)_{initial}{}^*[NAD(P)H]$$

$$\text{Turnover number (TON)} = [NAD(P)^+]/[Catalyst]$$

$$\text{Turnover frequency (TOF)} = \text{Turnover number/time (h)}$$

Photocatalytic reactions of Ir2 with amino acids: During the reaction of **Ir2** (1 μM) with various amino acids (20 mg/mL) in PBS solution at 298 K (in the dark for 30 min or after 5 min 465 nm light irradiation (11.7 J/cm^2)), H_2O_2 generation was detected by the peroxide test sticks.

Determination of singlet oxygen generation: The production of photo-induced singlet oxygen by the complexes was detected using the fluorescent sensor, 9,10-anthracenediyl-bis(methylene) dimalonic acid (ABDA). Briefly, **Ir1–Ir4** (1 μM) in H_2O was mixed with ABDA (100 μM). The solution was then placed in quartz cuvettes followed by 465 nm (11.7 J/cm^2) or 525 nm (29.56 J/cm^2) light irradiation for different times at 298 K. The absorbance of the ABDA was then monitored by UV-vis spectroscopy at 298 K.

Cell culture and dark- and photo-toxicity studies on monolayer tumor cells: HeLa, A431 and NP69 cell lines were maintained in DMEM medium supplemented with 10% fetal bovine serum, and 1% penicillin-streptomycin solution. B16 cell line was maintained in RPMI 1640 medium supplemented with 10% fetal bovine serum, and 1% penicillin-streptomycin solution. All cells were grown at 310 K in a humidified incubator under 5% CO_2 atmosphere.

Cell viability experiments were determined by MTT assay and performed in triplicate in 96-well flat bottom microtiter plates, where outer wells along the periphery contained 200 μL of PBS to minimize evaporation from sample wells. Cells were maintained in DMEM with 10% FBS and 1% penicillin-streptomycin solution. The number of healthy cells were calculated and then adjusted to 5×10^4 cells/mL with fresh medium. Cells were then transferred to inner wells containing 100 μL culture medium (5×10^3 cells per well), and placed in a 37 °C, 5% CO_2 incubator for 12 h to equilibrate and cell attachment. After the medium was removed completely, the cells were incubated with 100 μL fresh DMEM containing various concentrations of complexes. The final concentration of DMSO in all wells was lower than 0.1% (v/v). 100 μL drug free medium was added to the control wells. After incubation for 4 h with a series of concentrations of complexes, the medium was removed and replaced by fresh medium and the light groups were on 5 min irradiation at 465 nm (11.7 J/cm^2) or 525 nm (29.56 J/cm^2, LED light wavelength 460–590 nm with maximum at 525 nm, PURI Materials, China). After the incubation at 37 °C under 5% CO_2 for 44 h, 10 μL MTT solution (5 mg/mL) was added to each well, and cells were incubated for an additional 4 h. The medium was carefully removed and 100 μL DMSO was added to each well. After incubated for 10 min with shaking, the absorbance at 595 nm was recorded using Epoch™ Microplate Spectrophotometer (BioTek).

Flow cytometry analysis

In vitro cellular uptake assays: HeLa cells were inoculated into 12-well plate at the density of 10000 cells/mL and incubated for 48 h. **Ir1**, **Ir2** and **Ir3** of different concentrations (15 μM, 10 μM, 5 μM) were added to the wells and cultured for 0 h, 2 h and 4 h. The cells were collected by centrifugation, washed twice by PBS and underwent flow cytometric analysis (CytoFLEX of Beckman Coulter).

In vitro cellular retention assays: HeLa cells were inoculated into 12-well plate at the density of 10000/mL and incubated for 48 h. **Ir1**, **Ir2** and **Ir3** of different concentrations (15 μM, 10 μM, 5 μM) were added to the wells and cultured for 4 h. Then, the medium was removed and fresh medium was added. Subsequently, cells were collected at 0 h, 2 h, 4 h and 6 h respectively and washed twice by PBS and finally analyzed by flow cytometry (CytoFLEX of Beckman Coulter).

Cell uptake mechanism: The cells treated with the inhibitors and complexes **Ir1**–**Ir3** were washed, and the extent of uptake was analyzed by flow cytometry (CytoFLEX of Beckman Coulter). The cells were incubated with **Ir1**–**Ir3** (5 μM) for 2 h at 37 °C as the control. For metabolic inhibition, the cells were incubated at 4 °C for 1 h or incubated with 2-deoxy-D-glucose (50 mM) or oligomycin (5 μM) in PBS for 1 h at 37 °C. The cells were then incubated with complexes **Ir1**–**Ir3** (5 μM) for 2 h at 4 or 37 °C. For endocytic inhibition, the HeLa cells were pre-incubated with NH_4Cl (50 mM) or chlorpromazine (10 μM) in PBS for 1 h at 37 °C. The cells were then washed with PBS and incubated with complexes **Ir1**–**Ir3** (5 μM) for 2 h at 37 °C. For modulation of the membrane potential, the HeLa cells were pretreated with high K^+-HBSS (containing 170 mM K^+) to depolarize the cells or HBSS (containing 5.8 mM K+ and valinomycin (50 μM)) to hyperpolarize the cells for 1 h at 37 °C and then cells were incubated with complexes **Ir1**–**Ir3** (5 μM) for 2 h at 37 °C. Subsequently, the cells were collected, washed twice by PBS and finally analyzed by flow cytometry (CytoFLEX of Beckman Coulter).

Cellular localization assays: HeLa cells were seeded in a glass-bottom dish (Costar) at 310 K in a 5% CO_2 incubator. After 48 h, the cells were incubated with complexes **Ir1**–**Ir3** (10 μM) at 310 K for 2 h and further stained with Lyso- and Mito-Tracker (100 nM) for 20 min. Cell imaging was carried out immediately by confocal microscopy (LCSM 880, Carl Zeiss, Göttingen, Germany) with a 63× oil-immersion objective lens. **Ir1**–**Ir3** was excited at 488 nm, Lyso- and Mito- Tracker were excited at 633 nm. The phosphorescence/fluorescence was collected at 600 ± 20 nm, 680 ± 20 nm and 680 ± 20 nm for complexes, Lyso- and Mito-Tracker, respectively.

Determination of intracellular superoxide anion ($O_2^{<M->}$) levels: HeLa cells were seeded in 96-well plate at the density of 5000 cells per well and incubated for 48 h. After that, cells were incubated with **Ir1**–**Ir3** (0.01 μM) at 310 K for 4 h. The light groups were then on 5 min irradiation at 465 nm (11.7 J/cm^2). After that, the cells were incubated with 5 μM of dihydroethidium (DHE) for 30 min. Cell imaging was carried out then immediately by an inverted fluorescence microscope.

Mitochondrial membrane potentials ($\Delta\Psi_m$) assays: The mitochondrial membrane potential was determined by JC-1 assay. HeLa cells were seeded in 96-well plate at the density of 5000 cells per well for 48 h. Cells were incubated with **Ir2** at 310 K for 4 h. Then the medium was removed and replaced by fresh medium and the light groups were on 5 min irradiation at 465 nm (11.7 J/cm^2). After that, cells were incubated in 310 K, 5% CO_2 incubator for another 2 h. Then the cells were stained with JC-1 (2.5 μg/mL) at 310 K for 20 min and washed twice with PBS. The cells were imaged by an inverted fluorescence microscope.

Annexin V-FITC/PI assays: Mode of cell death was detected by Annexin V-FITC/PI dual staining. HeLa cells were seeded in 96-well plate for 48 h. The cells were treated with **Ir1**–**Ir3** at 310 K for 4 h. Then the medium was removed and replaced by fresh medium. Following this, the light groups were on 5 min irradiation at 465 nm (11.7 J/cm^2). After that, cells were incubated in 310 K, 5% CO_2 incubator for 2 h and subsequently stained with 5 μL of annexin V-FITC and 5 μL of PI stock solution in the dark for 30 min at 310 K. The fluorescence images were then obtained on an inverted fluorescence microscope.

In vivo PDT evaluation in A431 mice: Nude mice were purchased from Liaoning Changsheng Biotechnology Co. Ltd. This work was conducted in according with Animal Care and Institutional Ethical Guidelines in China. And all animal experiments were carried out under the permission by the Ethic Committee of Shenzhen University (certificate number: SYXK 2014-0140). Five million A431 cancer cells in 25 μL PBS and 25 μL matrige gel were subcutaneously injected to the right back of each mouse. 7 days after injection, the mice whose tumor volumes reached about 100 mm^3 were selected for further experiments. For the in vivo PDT experiments, twenty A431 tumor bearing nude mice were randomly divided into 4 groups (n = 5 per group) for various treatments:

(1) Control (intratumor injection, PBS),
(2) **Ir2** (intratumor injection, 0.86 mg/kg **Ir2**),
(3) Only Laser (intratumor injection, PBS; 465 nm, 26 mW/cm^2, 60 min),
(4) **Ir2** + Laser (intratumor injection, 0.86 mg/kg **Ir2**; 465 nm, 26 mW/cm^2, 60 min).

Tumor sizes were monitored every two days. The tumor volumes were calculated by the formula: volume = 0.5 × length × width^2. For H&E and TUNEL staining, tumors were collected at 24 h post treatment.

Acknowledgements

We appreciate the financial support from the National Natural Science Foundation of China (NSFC 22007104), the Guangdong Basic and Applied Basic Research Foundation (2019A1515110601, 2021B1515020050), Science, Technology and Innovation Commission of Shenzhen Municipality Project (JCYJ20190807152616996), the "Summit Plan" High level hospital construction project of Foshan (FSSYKF-2020002), DST, Government of India (DST/INSPIRE/04/2019/000492) and the U.S. National Science Foundation-grant (CHE-1764264).

Conflict of Interest

The authors declare no conflict of interest.

Keywords: anticancer · iridium complex · NADH · photo catalysis · photodynamic therapy

[1] C. A. Rabik, M. E. Dolan, *Cancer Treat. Rev.* **2007**, *33*, 9–23.
[2] D.-W. Shen, L. M. Pouliot, M. D. Hall, M. M. Gottesman, *Pharmacol. Rev.* **2012**, *64*, 706–721.
[3] A. M. Aparicio, A. L. Harzstark, P. G. Corn, S. Wen, J. C. Araujo, S.-M. Tu, L. C. Pagliaro, J. Kim, R. E. Millikan, C. Ryan, N. M. Tannir, A. J. Zurita, P. Mathew, W. Arap, P. Troncoso, P. F. Thall, C. J. Logothetis, *Clin. Cancer Res.* **2013**, *19*, 3621–3630.
[4] E. Pujade-Lauraine, S. Banerjee, S. Pignata, *J. Clin. Oncol.* **2019**, *37*, 2437–2448.
[5] H. Sung, J. Ferlay, R. L. Siegel, M. Laversanne, I. Soerjomataram, A. Jemal, F. Bray, *Ca-Cancer J. Clin.* **2021**, *71*, 209–249.
[6] P. Agostinis, K. Berg, K. A. Cengel, T. H. Foster, A. W. Girotti, S. O. Gollnick, S. M. Hahn, M. R. Hamblin, A. Juzeniene, D. Kessel, M. Korbelik, J. Moan, P. Mroz, D. Nowis, J. Piette, B. C. Wilson, J. Golab, *Ca-Cancer J. Clin.* **2011**, *61*, 250–281.
[7] X. Li, J. F. Lovell, J. Yoon, X. Chen, *Nat. Rev. Clin. Oncol.* **2020**, *17*, 657–674.
[8] U. Chilakamarthi, L. Giribabu, *Chem. Rec.* **2017**, *17*, 775–802.
[9] C. Richert, J. M. Wessels, M. Mueller, M. Kisters, T. Benninghaus, A. E. Goetz, *J. Med. Chem.* **1994**, *37*, 2797–2807.
[10] N. Lange, M. Zellweger, M. Forrer, A. Marti, L. Guillou, P. Kucera, G. Wagnières, H. Bergh, *Br. J. Cancer* **1999**, *80*, 185–193.
[11] W. Yu, W. Zhen, Q. Zhang, Y. Li, H. Luo, J. He, Y. Liu, *ChemMedChem* **2020**, *15*, 1766–1775.
[12] E. C. Fiedler, M. T. Hemann, *Annu. Rev. Cancer Biol.* **2019**, *3*, 409–428.
[13] H. Shi, P. J. Sadler, *Br. J. Cancer* **2020**, *123*, 871–873.
[14] a) J. A. Roque III, P. C. Barrett, H. D. Cole, L. M. Lifshits, G. Shi, S. Monro, D. V. Dohlen, S. Kim, N. Russo, G. Deep, C. G. Cameron, M. E. Alberto, S. A. McFarland, *Chem. Sci.* **2020**, *11*, 9784–9806; b) J. A. Roque III, P. C. Barrett, H. D. Cole, L. M. Lifshits, E. Bradner, G. Shi, D. V. Dohlen, S. Kim, N. Russo, G. Deep, C. G. Cameron, M. E. Alberto, S. A. McFarland, *Inorg. Chem.* **2020**, *59*, 16341–16360.
[15] a) X. Li, N. Kwon, Tian. Guo, Z. Liu, J. Yoon, *Angew. Chem. Int. Ed.* **2018**, *57*, 11522–11531; *Angew. Chem.* **2018**, *130*, 11694–11704; b) S. Geri, T. Krunclova, O. Janouskova, J. Panek, M. Hruby, D. Hernández-Valdés, B. Probst, R. A. Alberto, C. Mamat, M. Kubeil, H. Stephan, *Chem. Eur. J.* **2020**, *26*, 10992–11006.
[16] a) C. Imberti, P. Zhang, H. Huang, P. J. Sadler, *Angew. Chem. Int. Ed.* **2020**, *59*, 61–73; *Angew. Chem.* **2020**, *132*, 61–73; b) W. Sun, R. Thiramanas, L. D. Slep, X. Zeng, V. Mailänder, S. Wu, *Chem. Eur. J.* **2017**, *23*,10832–10837; c) B. F. Hohlfeld, B. Gitter, C. J. Kingsbury, K. J. Flanagan, D. Steen, G. D. Wieland, N. Kulak, M. O. Senge, A. Wiehe, *Chem. Eur. J.* **2021**, *27*, 6440–6459.
[17] P. Zhang, H. Huang, S. Banerjee, G. J. Clarkson, C. Ge, C. Imberti, P. J. Sadler, *Angew. Chem. Int. Ed.* **2019**, *58*, 2350–2354; *Angew. Chem.* **2019**, *131*, 2372–2376.
[18] S. Monro, K. L. Colón, J. Roque III, P. Konda, S. Gujar, R. P. Thummel, L. Lilge, C. G. Cameron, S. A. McFarland, *Chem. Rev.* **2019**, *119*, 797–828.
[19] S. A. McFarland, A. Mandel, R. Dumoulin-White, G. Gasser, *Curr. Opin. Chem. Biol.* **2020**, *56*, 23–27.
[20] D. A. Smithen, S. Monro, M. Pinto, J. Roque III, R. M. Diaz-Rodriguez, H. Yin, C. G. Cameron, A. Thompson, S. A. McFarland, *Chem. Sci.* **2020**, *11*, 12047–12069.
[21] a) J. Karges, U. Basu, O. Blacque, H. Chao, G. Gasser, *Angew. Chem. Int. Ed.* **2019**, *58*, 14334–14340; *Angew. Chem.* **2019**, *131*, 14472–14478; b) B. Liu, J. Jiao, W. Xu, M. Zhang, P. Cui, Z. Guo, Y. Deng, H. Chen, W. Sun, *Adv. Mater.* **2021**, *33*, 2100795.
[22] a) V. Novohradsky, A. Rovira, C. Hally, A. Galindo, G. Vigueras, A. Gandioso, M. Svitelova, R. Bresolí-Obach, H. Kostrhunova, L. Markova, J. Kasparkova, S. Nonell, J. Ruiz, V. Brabec, V. Marchán, *Angew. Chem. Int. Ed.* **2019**, *58*, 6311–6315; *Angew. Chem.* **2019**, *131*, 6377–6381; b) J. Karges, F. Heinemann, M. Jakubaszek, F. Maschietto, C. Subecz, M. Dotou, R. Vinck, O. Blacque, M. Tharaud, B. Goud, E. V. Zahínos, B. Spingler, I. Ciofini, G. Gasser, *J. Am. Chem. Soc.* **2020**, *142*, 6578–6587.
[23] a) H. Huang, S. Banerjee, K. Qiu, P. Zhang, O. Blacque, T. Malcomson, M. J. Paterson, G. J. Clarkson, M. Staniforth, V. G. Stavros, G. Gasser, H. Chao, P. J. Sadler, *Nat. Chem.* **2019**, *11*, 1041–1048; b) S. Banerjee, P. J. Sadler, *RSC Chem. Biol.* **2021**, *2*, 12–29.
[24] a) C. Huang, C. Liang, T. Sadhukhan, S. Banerjee, Z. Fan, T. Li, Z. Zhu, P. Zhang, K. Raghavachari, H. Huang, *Angew. Chem. Int. Ed.* **2021**, *60*, 9474–9479; b) Z. Fan, J. Huang, H. Huang, S. Banerjee, *ChemMedChem* **2021**, *16*, 2480–2486.
[25] S. Zhu, Z. Dong, X. Ke, J. Hou, E. Zhao, K. Zhang, F. Wang, L. Yang, Z. Xiang, H. Cui, *Semin. Cancer Biol.* **2019**, *57*, 59–71.
[26] C. Sun, X. Liu, B. Wang, Z. Wang, Y. Liu, C. Di, J. Si, H. Li, Q. Wu, D. Xu, J. Li, G. Li, Y. Wang, F. Wang, H. Zhang, *Theranostics* **2019**, *9*, 3595–3607.
[27] E. Gaude, C. Schmidt, P. A. Gammage, A. Dugourd, T. Blacker, S. P. Chew, J. Saez-Rodriguez, J. S. O'Neill, G. Szabadkai, M. Minczuk, C. Frezza, *Mol. Cell* **2018**, *69*, 581–593.
[28] D. V. Titov, V. Cracan, R. P. Goodman, J. Peng, Z. Grabarek, V. K. Mootha, *Science* **2016**, *352*, 231–235.
[29] J. Xu, H. Yang, W. Zhang, *Crit. Rev. Biotechnol.* **2018**, *38*, 1061–1076.
[30] Zhu, J. S. Schwörer, M. Berisa, Y. J. Kyung, K. W. Ryu, J. Yi, X. Jiang, J. R. Cross, *Science* **2021**, *372*, 968–972.
[31] G. M. Rather, A. A. Pramono, Z. Szekely, P. M. Tedeschi, *Pharmacol. Ther.* **2021**, *226*, 107864.
[32] Z. Liu, P. J. Sadler, *Acc. Chem. Res.* **2014**, *47*, 1174–1185.
[33] J. J. Soldevila-Barreda, N. Metzler-Nolte, *Chem. Rev.* **2019**, *119*, 829–869.
[34] a) Q. Zhang, X. Lu, H. Wang, X. Tian, A. Wang, H. Zhou, J. Wu, Y. Tian, *Chem. Commun.* **2018**, *54*, 3771–3774; b) Z. Jin, S. Qi, X. Guo, N. Tian, Y. Hou, C. Li, X. Wang, Q. Zhou, *Chem. Commun.* **2020**, *56*, 2845–2848; c) X. Tian, Y. Zhu, M. Zhang, L. Luo, J. Wu, H. Zhou, L. Guan, G. Battaglia, Y. Tian, *Chem. Commun.* **2017**, *53*, 3303–3306; d) V. Singh, D. R. P. Paitandi, B. K. Dwivedi, R. S. Singh, D. S. Pandey, *Organometallics* **2018**, *37*, 3827–3838.
[35] A. Pons, L. Delion, T. Poisson, A. B. Charette, P. Jubault, *Acc. Chem. Res.* **2021**, *54*, 2969–2990.
[36] a) T. A. Matias, A. P. Mangoni, S. H. Toma, F. N. Rein, R. C. Rocha, H. E. Toma, K. Araki, *Eur. J. Inorg. Chem.* **2017**, *4*, 768–768; b) S.-y. Takizawa, N. Ikuta, F. Zeng, S. Komaru, S. Sebata, S. Murata, *Inorg. Chem.* **2016**, *55*, 8723–8735; c) C. Dragonetti, L. Falciola, P. Mussini, S. Righetto, D. Roberto, R. Ugo, A. Valore, F. D. Angelis, S. Fantacci, A. Sgamellotti, M. Ramon, M. Muccini, *Inorg. Chem.* **2007**, *46*, 8533–8547.
[37] F. Zhang, D. Ma, L. Duan, J. Qiao, G. Dong, L. Wang, Y. Qiu, *Inorg. Chem.* **2014**, *53*, 6596–6606.
[38] C. Li, S. Wang, Y. Huang, Q. Wen, L. Wang, Y. Kan, *Dalton Trans.* **2014**, *43*, 5595–5602.
[39] W. J. Finkenzeller, H. Yersin, *Chem. Phys. Lett.* **2003**, *377*, 299–305.
[40] T. Entradas, S. Waldron, M. Volk, *J. Photochem. Photobiol. B* **2020**, *204*, 111787.
[41] X. Chen, S. Li, L. Liu, *Trends Biotechnol.* **2014**, *32*, 337–343.
[42] J. Carmichael, W. G. DeGraff, A. F. Gazdar, J. D. Minna, J. B. Mitchell, *Cancer Res.* **1987**, *47*, 936–942.
[43] Y. Yang, L. Guo, Z. Tian, Y. Gong, H. Zheng, S. Zhang, Z. Xu, X. Ge, Z. Liu, *Inorg. Chem.* **2018**, *57*, 11087–11098.
[44] C. Liu, X. Liu, X. Ge, Q. Wang, L. Zhang, W. Shang, Y. Zhang, X. A. Yuan, L. Tian, Z. Liu, J. You, *Dalton Trans.* **2020**, *49*, 5988–5998.
[45] M. M. Haghdoost, G. Golbaghi, M. Létourneau, S. A. Patten, A. Castonguay, *Eur. J. Med. Chem.* **2017**, *132*, 282–293.
[46] M. M. Haghdoost, G. Golbaghi, J. Guard, S. Sielanczyk, S. A. Patten, A. Castonguay, *Dalton Trans.* **2019**, *48*, 13396–13405.
[47] Y. Zhang, S. Zhang, Z. Tian, J. Li, Z. Xu, S. Li, Z. Liu, *Dalton Trans.* **2018**, *47*, 13781–13787.
[48] Z. H. Siddik, *Oncogene* **2003**, *22*, 7265–7279.
[49] S. P. Oldfield, M. D. Hall, J. A. Platts, *J. Med. Chem.* **2007**, *50*, 5227–5237.
[50] M. Sabbatini, I. Zanellato, M. Ravera, E. Gabano, E. Perin, B. Rangone, D. Osella, *J. Med. Chem.* **2019**, *62*, 3395–3406.
[51] F. Zhao, Y. Zhao, Y. Liu, X. Chang, C. Chen, Y. Zhao, *Small* **2011**, *7*, 1322–1337.
[52] H. M. Kalckar, *Chem. Rev.* **1941**, *28*, 71–178.

[53] C. A. Puckett, J. K. Barton, *Biochemistry* **2008**, *47*, 11711–11716.
[54] M. Ouyang, L. Zeng, H. Huang, C. Jin, J. Liu, Y. Chen, L. Ji, H. Chao, *Dalton Trans.* **2017**, *46*, 6734–6744.
[55] W. Huang, Z. Chen, L. Hou, P. Feng, Y. Li, T. Chen, *Dalton Trans.* **2020**, *49*, 11556–11564.
[56] S. Kwon, H. Ko, D. G. You, K. Kataoka, J. H. Park, *Acc. Chem. Res.* **2019**, *52*, 1771–1782.
[57] C. Huang, T. Li, J. Liang, H. Huang, P. Zhang, S. Banerjee, *Coord. Chem. Rev.* **2020**, *408*, 213178.
[58] N. Tian, W. Sun, X. Guo, J. Lu, C. Li, Y. Hou, X. Wang, Q. Zhou, *Chem. Commun.* **2019**, *55*, 2676–2679.
[59] D. Nolfi-Donegan, A. Braganza, S. Shiva, *Redox Biol.* **2020**, *37*, 101674.
[60] J. Chen, S. C. Rogers, M. Kavdia, *Ann. Biomed. Eng.* **2013**, *41*, 327–337.
[61] A. Perelman, C. Wachtel, M. Cohen, S. Haupt, H. Shapiro, A. Tzur, *Cell Death Dis.* **2012**, *22*, e430.
[62] E. Gottlieb, S. M. Armour, M. H. Harris, C. B. Thompson, *Cell Death Differ.* **2003**, *10*, 709–717.
[63] J. D. Ly, D. R. Grubb, A. Lawen, *Apoptosis* **2003**, *8*, 115–128.
[64] M. J. Frisch, G. W. Trucks, H. B. Schlegel, G. E. Scuseria, M. A. Robb, J. R. Cheeseman, G. Scalmani, V. Barone, G. A. Petersson, H. Nakatsuji, X. Li, M. Caricato, A. V. Marenich, J. Bloino, B. G. Janesko, R. Gomperts, B. Mennucci, H. P. Hratchian, J. V. Ortiz, A. F. Izmaylov, J. L. Sonnenberg, D. Williams-Young, F. Ding, F. Lipparini, F. Egidi, J. Goings, B. Peng, A. Petrone, T. Henderson, D. Ranasinghe, V. G. Zakrzewski, J. Gao, N. Rega, G. Zheng, W. Liang, M. Hada, M. Ehara, K. Toyota, R. Fukuda, J. Hasegawa, M. Ishida, T. Nakajima, Y. Honda, O. Kitao, H. Nakai, T. Vreven, K. Throssell, J. A. Montgomery Jr., J. E. Peralta, F. Ogliaro, M. J. Bearpark, J. J. Heyd, E. N. Brothers, K. N. Kudin, V. N. Staroverov, T. A. Keith, R. Kobayashi, J. Normand, K. Raghavachari, A. P. Rendell, J. C. Burant, S. S. Iyengar, J. Tomasi, M. Cossi, J. M. Millam, M. Klene, C. Adamo, R. Cammi, J. W. Ochterski, R. L. Martin, K. Morokuma, O. Farkas, J. B. Foresman, D. J. Fox, *Gaussian 16* Rev. C.01, Wallingford, CT, **2016**.

Manuscript received: September 15, 2021
Accepted manuscript online: November 10, 2021
Version of record online: December 2, 2021